3 THE ANTARES NEUTRINO TELESCOPE

In this chapter a description of the whole detection process is given, starting from a neutrino interacting in the vicinity of the detector, to the arrival of the data at the shore station. The ANTARES detector uses the so-called *all-data-to-shore* concept, which means that all signals that are recorded by the PMTs are sent to shore and could in principle be stored. Since this would require too much storage space, non-interesting signals are directly filtered out in a process called *triggering*. This procedure, and the reconstruction of the neutrino interaction from the signals measured by the PMTs are described in chapter 4.

First the neutrino interactions and light production by the interaction products are described in section 3.1. A description is also given of the sources of optical background present in the deep sea. Following this, the ANTARES detector is introduced in section 3.2, and details of its components are given. For an exhaustive description of the detector, see the paper by Ageron et al. [2011].

3.1 NEUTRINO SIGNATURES

Neutrinos only interact via the weak interaction by exchanging a weak boson with a target nucleus in the water around or the rock below the ANTARES detector. If a charged W-boson is exchanged the interaction is called a Charged Current (CC) interaction; if a neutral Z-boson is exchanged it is called a Neutral Current (NC) interaction, see figure 3.1. In a NC interaction, the neutrino interaction may break up the nucleus, which induces a hadronic shower with a size depending on its energy (a typical size being a few metres). Not all of the energy of the neutrino is transferred to the nucleus, and the outgoing neutrino carries away an (unknown) part of the total energy, depending on the elasticity of the interaction. Because of this, the energy resolution of these interactions is very poor. About 1 in 4 neutrino interactions proceeds via the neutral current (see the right plot in figure 3.2).

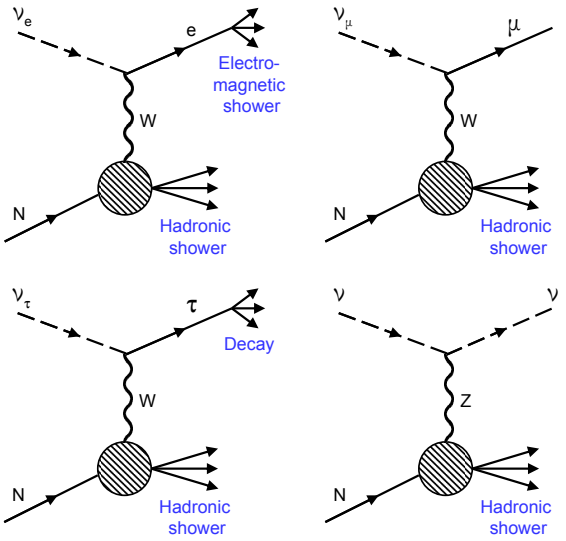

Figure 3.1: The different neutrino interactions. TOP LEFT: CC electron-neutrino. TOP RIGHT: CC muon-neutrino. BOTTOM LEFT: CC tau-neutrino. BOTTOM RIGHT: NC.

In a CC interaction, in addition to a hadronic shower, the exact signature produced depends on the neutrino flavour, see figure 3.1. In a CC interaction of an electron-neutrino[17] an electron is produced, which in turn produces an electromagnetic shower due to bremsstrahlung and pair production. The size of this shower again depends on its energy. In a CC muon-neutrino interaction a muon is produced, which has a much larger mass, meaning that the energy losses due to bremsstrahlung and pair production are reduced. Due to its relatively long mean life time of about 2.2 µs, the muon travels a considerable distance before decaying. Finally, in a CC tau-neutrino interaction a tau is produced, which has a much shorter mean life time τ_τ of about $2.9 \cdot 10^{-7}$ µs.

[17] *An anti-electron-neutrino will create a positron, but the interaction will otherwise look the same.*

The average distance d between the interaction and the decay vertex for the tau is given by:

$$d = \frac{E_\tau \tau_\tau}{m_\tau c}, \tag{3.1}$$

where E_τ and m_τ are the energy and mass of the tau particle respectively. Using $m_\tau = 1.78\,\mathrm{GeV}/c^2$ gives $d = 4.9$ m for a 100 TeV tau particle. Except for energies above 100 TeV, the interaction vertex and the decay vertex cannot be separated in ANTARES sufficiently well to detect a tau-neutrino signature.

The tau can decay in various ways:

$$\begin{aligned} &\text{A. } \tau^- \to \text{Hadrons} && (\sim 65\%) \\ &\text{B. } \tau^- \to e^- + \overline{\nu}_e + \nu_\tau && (17.85\%) \\ &\text{C. } \tau^- \to \mu^- + \overline{\nu}_\mu + \nu_\tau && (17.36\%) \end{aligned} \tag{3.2}$$

where A will create a hadronic shower and B an electromagnetic shower. In ANTARES, the muonic decay (C) cannot be distinguished from the muon-neutrino CC interaction and will therefore contribute to the CC muon channel.

Since neutrinos only interact via the weak interaction, their cross section is low compared to other processes. The neutrino-nucleon CC cross section is given by [Connolly et al., 2011]:

$$\sigma_{\nu N}^{CC} = \frac{2 G_F m_N E_\nu}{\pi} \int_0^1 \int_0^1 dx\, dy \left(\frac{M_W^2}{Q^2 + M_W^2} \right)^2 \left[q + (1-y)^2 \overline{q} \right], \tag{3.3}$$

where G_F is the Fermi coupling constant, m_N and M_W are the nucleon and W-boson mass respectively, $-Q^2$ is the square of the four-momentum transfer between the neutrino and the nucleon, q and $\overline{q}$ are the corresponding parton distribution functions for quarks and anti-quarks, x is the parton momentum fraction and y is the inelasticity. The neutrino-nucleon NC cross section is very similar:

$$\sigma_{\nu N}^{NC} = \frac{2 G_F m_N E_\nu}{\pi} \int_0^1 \int_0^1 dx\, dy \left(\frac{M_Z^2}{Q^2 + M_Z^2} \right)^2 \left[q^0 + (1-y)^2 \overline{q}^0 \right], \tag{3.4}$$

where M_Z is the Z-boson mass and q^0 and $\overline{q}^0$ are the sum of all parton distribution functions, since the Z-boson can interact with any quark.

The neutrino-nucleon cross sections are shown in figure 3.2. The left plot shows the CC cross section for both muon-neutrinos and anti-muon-neutrinos, from which it can be seen that the former is about a factor of two higher. This is due to the fact that neutrinos are predominantly left-handed, so that scattering on (right-handed) anti-quarks is suppressed compared to scattering on (left-handed) quarks and by the larger momentum fraction carried by quarks [McFarland, 2008]. The right plot in the figure shows the muon-neutrino CC and NC cross sections versus energy. The NC cross section is about a factor three lower than

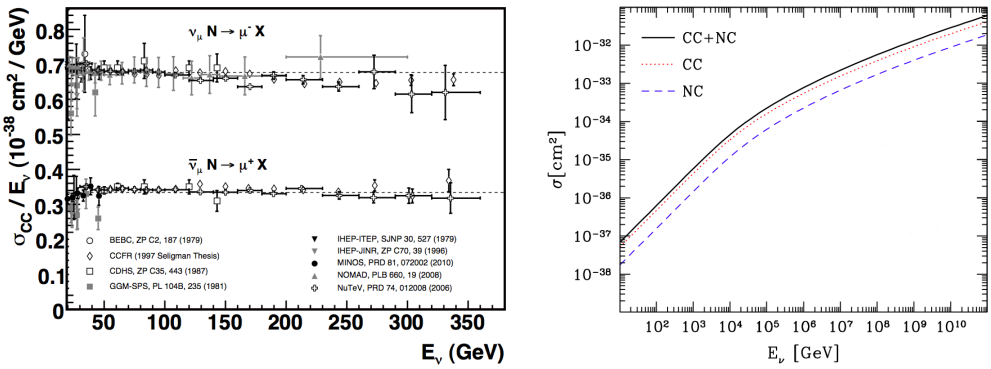

Figure 3.2: The neutrino-nucleon cross section versus neutrino energy. LEFT: the CC for muon-(anti-)neutrinos (divided by neutrino energy) up to 350 GeV. Figure reproduced from Formaggio and Zeller [2013]. RIGHT: both CC and NC for the average of muon-neutrinos and anti-neutrinos. Figure reproduced from Ahlers et al. [2006].

the CC cross section due to the difference in the W- and Z-boson mass and couplings [Paschos, 2002].

As pointed out before, only muon-(anti-)neutrinos are used for this work, and more specifically the CC interaction in which an (anti-)muon is produced. The average distance travelled by a muon with initial energy E_0 is given by:

$$R_\mu = \frac{1}{b(E_\mu)} \ln\left(1 + \frac{b(E_\mu)}{a(E_\mu)} E_0\right), \tag{3.5}$$

with $a(E_\mu)$ representing the ionisation losses and $b(E_\mu)$ the radiative losses. For water $a(E_\mu) \simeq 2.67\,\mathrm{MeV/cm}$ and $b(E_\mu) \simeq 3.4 \cdot 10^{-6}\,\mathrm{cm}^{-1}$. Above 100 GeV, the range of the muon exceeds 350 m. The muon thus has enough energy to traverse the detector (see figure 3.6), even if it is produced outside.

3.1.1 *Muon propagation*

While passing through the water or rock, the muon loses its energy by ionisation and radiative processes. The radiative processes, which consist of electron-positron pair production, bremsstrahlung and photonuclear contributions, are characterised by large energy fluctuations and become the dominant energy loss mechanism above several hundred GeV [Beringer et al., 2012]. The direction of the muon is subject to multiple Coulomb scattering off atomic nuclei.

Since the muon is a charged particle, and at the energies of interest has a velocity higher than the phase velocity of light,

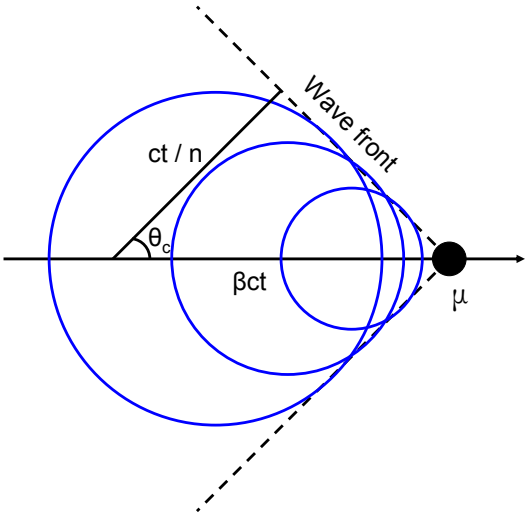

Figure 3.3: Schematic view of Čerenkov radiation.

Čerenkov radiation is produced [Čerenkov, 1937]. The charged particle polarises the atoms in the medium, resulting in the emission of dipole radiation at a specific angle θ_c (see also figure 3.3):

$$\cos\theta_c = \frac{1}{\beta n(\lambda)}, \tag{3.6}$$

where $\beta = v/c$ is the ratio between the velocity of the muon and the speed of light (in vacuum) and $n(\lambda)$ is the refractive index, which depends on the wavelength λ. Between 400 and 500 nm, which is the wavelength range of interest for ANTARES (see section 3.2.1), the refractive index of sea water is around 1.35 [Adrián-Martínez et al., 2012c]. For the neutrino energies of interest, $\beta \simeq 1$ and the light is emitted at an angle of about 42°.

The number of photons emitted per unit track length x and per unit wavelength is [Beringer et al., 2012]:

$$\frac{\mathrm{d}^2 N_\gamma}{\mathrm{d}x\mathrm{d}\lambda} = \frac{2\pi\alpha Z^2}{\lambda^2}\left(1 - \frac{1}{\beta^2 n^2(\lambda)}\right), \tag{3.7}$$

where α is the fine structure constant. Although the emission of photons constitutes a form of energy loss for the muon, it is small compared to ionisation and radiative processes [Allison and Wright, 1984]. Between 400 and 500 nm, about 100 photons are emitted per centimetre of track length.

The path of the muon yields a long lever arm, so the direction of the muon can in principle be well reconstructed. Furthermore, the

muon direction is effectively the same as the neutrino direction above energies of about 100 TeV, see figure 3.4. Below about 10 TeV the angular resolution is dominated by the angle between the muon and the neutrino in the neutrino interaction [Amram et al., 1999].

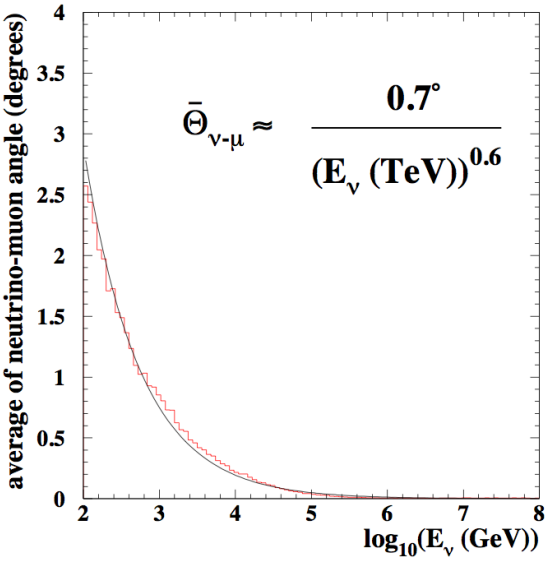

Figure 3.4: The average angle between the directions of the neutrino and the muon. Figure reproduced from [Amram et al., 1999].

The propagation of Čerenkov light through the sea water is affected by absorption and scattering. The intensity of the emitted light as a function of distance can be written as [Aguilar et al., 2005]:

$$I(s,\lambda) = I_0\, e^{-s/\lambda_{\text{att}}^{\text{eff}}(\lambda)}, \tag{3.8}$$

where I_0 is the intensity of the emitted light, s is the optical path length and $\lambda_{\text{att}}^{\text{eff}}(\lambda)$ is the effective attenuation length given by:

$$\frac{1}{\lambda_{\text{att}}^{\text{eff}}(\lambda)} = \frac{1}{\lambda_{\text{abs}}(\lambda)} + \frac{1}{\lambda_{\text{scat}}^{\text{eff}}(\lambda)}, \tag{3.9}$$

where $\lambda_{\text{abs}}(\lambda)$ is the absorption length and $\lambda_{\text{scat}}^{\text{eff}}(\lambda)$ is the effective scattering length, which is given by:

$$\lambda_{\text{scat}}^{\text{eff}} = \frac{\lambda_{\text{scat}}}{1 - \langle \cos\theta_{\text{scat}} \rangle}, \tag{3.10}$$

with $\langle \cos\theta_{\text{scat}} \rangle$ the average cosine of the scattering angle, which peaks in the forward direction and has a value of about 0.9. The

effective scattering length is a more useful quantity than the scattering length, since a photon that is scattered under a very small angle will only be delayed a little bit.

The absorption length of ice is longer than that of water, but the attenuation length is shorter, because the scattering length in ice is shorter. This leads to a worse angular resolution in ice, which is important for astronomy. More on the angular resolution can be found in chapter 4.

For ANTARES, the absorption length is about 60 m at a wavelength of 475 nm, while the effective scattering length is about 265 m [Aguilar et al., 2005].

Optical background

In addition to the Čerenkov photons produced by a muon, there are other sources of light in the deep sea. One of the sources is the decay of ^{40}K. This radioactive isotope of potassium has a very long half-life of $1.248 \cdot 10^9$ year and has a natural abundance of 0.012%; i. e. 120 out of one million potassium atoms will be ^{40}K. It can decay via all three channels:

$$\begin{aligned} {}^{40}\mathrm{K} &\rightarrow {}^{40}\mathrm{Ca} + \mathrm{e}^- + \overline{\nu}_\mathrm{e} && (89.28\%) \\ {}^{40}\mathrm{K} + \mathrm{e}^- &\rightarrow {}^{40}\mathrm{Ar} + \gamma + \nu_\mathrm{e} && (10.72\%) \\ {}^{40}\mathrm{K} &\rightarrow {}^{40}\mathrm{Ar} + \mathrm{e}^+ + \nu_\mathrm{e} && (\sim 0.001\%) \end{aligned} \tag{3.11}$$

The electron produced in the decay to ^{40}Ca has an energy up to 1.33 MeV, which is above the Čerenkov threshold for electrons in water (0.26 MeV) and produces up to 150 Čerenkov photons. The photon in the electron-capture process has an energy of 1.46 MeV and Čerenkov photons can be produced by electrons via Compton scattering of the photon.

Another source of light production is luminescence from organisms present in the water, so-called bioluminescence. The amount of light produced can be several orders higher than that produced by the ^{40}K-decay, but generally occurs in short bursts of light.

No radioactive ^{40}K or luminescent organisms are present in ice and the only (optical) background for a detector in ice is that created by the detector itself [Halzen and Klein, 2010].

3.2 THE ANTARES DETECTOR

The ANTARES neutrino telescope is located 40 km offshore from Toulon, France, see figure 3.5. Its coordinates are 42°48′ N, 6°10′ E.

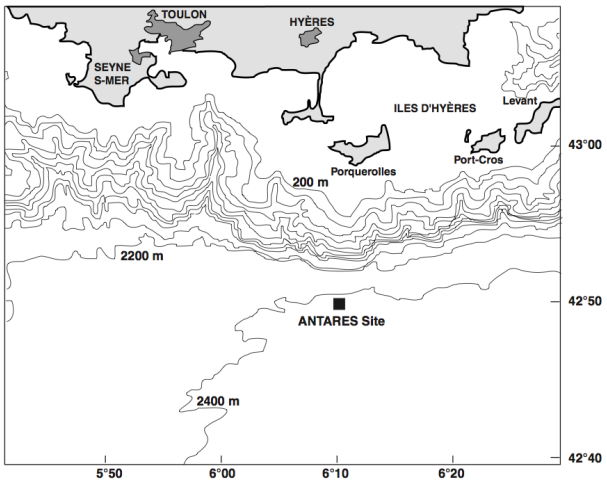

Figure 3.5: Map of the ANTARES site near Toulon. Figure reproduced from Amram et al. [1999].

The detector is located at a depth of 2475 m below sea level and consists of 12 lines. The first 11 lines consist of 25 storeys with a triplet of so-called Optical Modules (see below) and line number 12 consists of 20 storeys. The top part of this line contains acoustic detection devices.

Each line is divided in sectors, containing five storeys each, which have independent power distribution and data communication. This makes it possible to use part of the string in case of a failure. The different components of ANTARES will now be described in more detail; for a schematic overview of the detector, see figure 3.6.

3.2.1 *The optical module*

The photons are detected by PhotoMultiplier Tubes (PMTs), which are housed in a glass sphere called the Optical Module (OM). A PMT detects light using the photo-electric effect, whereby a photon liberates an electron from the photocathode, which is accelerated (and multiplied) in an electric field. It provides a current output proportional to the light intensity.

After considering several commercially available models, the 10″ Hamamatsu R7081-20 PMT was chosen, which is sensitive for light in the wavelength range of $300 - 600$ nm, with a maximum quantum efficiency of about 22% between 350 and 450 nm. The OM is the building block of the detector, which contains a total

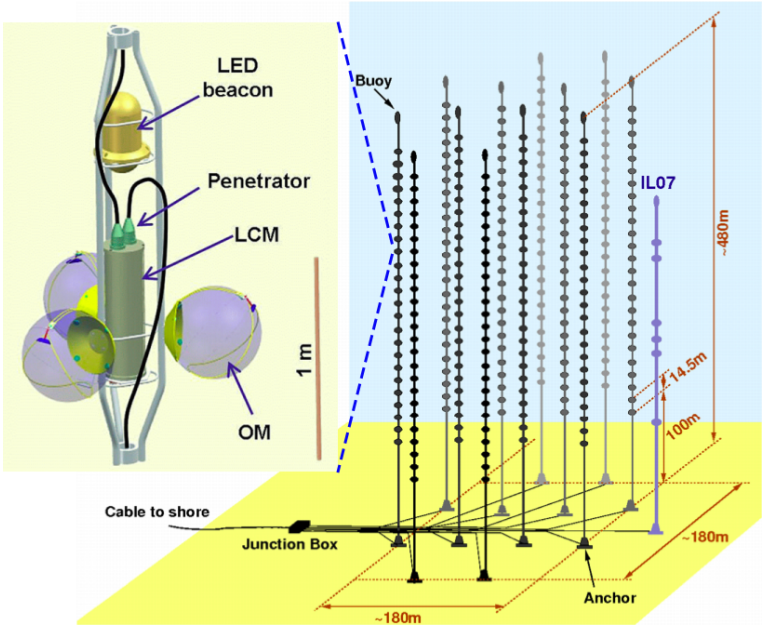

Figure 3.6: Schematic overview of the ANTARES detector, the inset shows a schematic view of a storey. Figure reproduced from Ageron et al. [2011].

of 885 OMs distributed over the 12 lines. The OMs look downward at an angle of 45° below the horizon in order to optimise the detection of light from upgoing muons. Figure 3.7 shows a schematic view and a photograph of an assembled OM.

A key parameter of the PMT is the Transit Time Spread (TTS). The transit time is the time it takes the photo-electron to traverse the PMT. It varies from electron to electron, which is summarised by the TTS, which is the standard deviation of the transit time distribution. From earlier studies it was found that a TTS of 1.5 ns is needed to obtain a sub-degree angular resolution. The chosen PMT has an average TTS of about 1.3 ns, which is conform the requirements [Amram et al., 2002].

The PMT is shielded against the Earth's magnetic field (~0.46 G locally) using a so-called μ-metal cage. Without this shielding, the TTS and charge amplification of the PMT would be significantly degraded. The PMT and the μ-metal cage are held in place in the OM with optical gel. The OM also contains an LED, which is used to monitor the internal timing of the OM (see section 3.2.5). The high voltage is generated by an electronics board mounted on the base, which is connected to an electronics container via a penetrator.

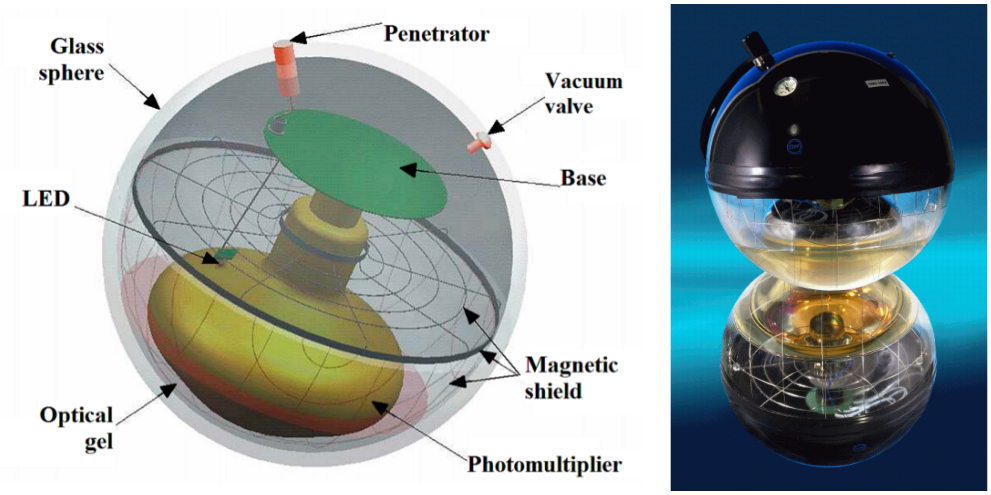

Figure 3.7: The ANTARES optical module. Figures reproduced from Ageron et al. [2011]. LEFT: schematic view. RIGHT: photograph.

An example of the output produced by a PMT is shown in figure 3.8, in which the counting rate is shown versus time. The base line in the counting rate, shown as a red dashed line, can be attributed to potassium decay and dark noise produced by the PMT. A typical value for the base line is 60 kHz (see also figure 4.4), but in this case it is just above 40 kHz. This difference can be attributed to the different quantum efficiencies of the PMTs. The short term bursts (lasting up to tens of seconds) are caused by bioluminescence.

3.2.2 *Detector layout*

In addition to three OMs, a storey also contains an electronics container, referred to as the Local Control Module (LCM), which houses the offshore electronics; see the inset in figure 3.6. The distance between storeys is 14.5 m, with the first storey being located about 100 m above the sea floor. The line is anchored by the Bottom String Socket (BSS) and held vertical by a buoy. The BSS consists of a dead weight which acts as an anchor, and a recoverable part that can be disconnected using an acoustic release. Once released, the line will float to the surface and can be picked up by a boat. The BSS also contains the String Control Module (SCM), which contains additional electronics.

An interlink cable links each line to the Junction Box (JB), which in turn is connected to the shore station by the Main Electro-

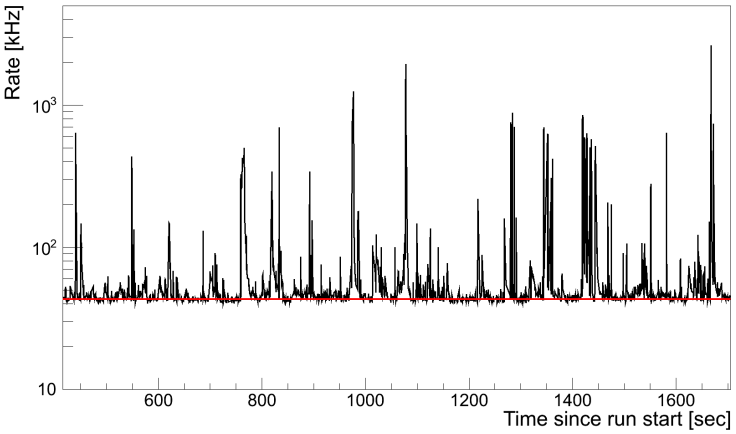

Figure 3.8: Example of the time dependence of the counting rate, the red line shows the base line.

Optical Cable (MEOC). After deployment of a line, an interlink cable is connected to the JB with a Remotely Operated underwater Vehicle (ROV). The MEOC is a standard telecommunications cable and provides the electrical power link and the optical data link between the detector and the shore station.

In addition to the twelve lines instrumented with OMs for the detection of neutrinos, there is a thirteenth line known as the Instrumentation Line (IL). This line contains several different instruments, including an acoustic detection system, instruments to monitor the speed and direction of the sea current, a sound velocimeter and cameras to record images of bioluminescent organisms.

Detector History

Construction of the detector commenced in 2001 with the installation of the MEOC, followed by the JB in December 2002. In March 2006, the first detector line was installed, followed by the second one in July 2006 and three more on January 29th 2007. With the connection of these lines ANTARES became the largest detector on the Northern Hemisphere.

In December of 2007, five more lines were installed, effectively doubling the size of the detector. The detector was completed on May 28th 2008 with the connection of lines 11 and 12. The detector did not always run with all twelve lines, since for some periods one or more of the lines exhibited problems and had to be recovered and repaired. From June 25th 2008 to September 5th

2008 the detector did not take any data due to a problem with the MEOC.

The full ANTARES detector collects on average about 5 atmospheric muons per second and about 3 neutrino candidates per day [Bogazzi, 2014].

3.2.3 *Data acquisition*

p.e.: photon-equivalent, the output signal of the PMT corresponding to the detection of one photon.

All signals from the PMTs that pass a predefined voltage threshold (typically equivalent to 0.3 p.e.) are digitised by an Analogue Ring Sampler (ARS) chip located in the LCM. The analogue signal is integrated by an Amplitude to Voltage Converter (AVC) to obtain the charge. The arrival time of the hit is determined by a Time to Voltage Converter (TVC) using the signal of the local clock, which is synchronised to a 20 MHz onshore master clock. Each LCM contains two ARSs which are connected to work in a token-ring scheme, to minimise the dead time induced by the digitisation. In the token-ring scheme, the ARS holding the token will treat the incoming events. After the signal integration the token is passed over to the other ARS with a delay of about $10 - 20$ ns [Aguilar et al., 2010].

In each sector of five OMs, one of the LCMs is the Master Local Control Module (MLCM). It multiplexes the signals from the other four storeys via an optical connection. The MLCM passes these multiplexed signals to a Dense Wavelength Division Multiplexer (DWDM) which in turn sends the data, via the MEOC, to shore. As noted before, no filtering of the data is performed, and all data from the OMs are sent to shore. Each MLCM uses a laser with a specific frequency chosen in the range from 192.1 to 194.9 THz, so that the data from the five sectors in a string can be transmitted to shore via a single fibre.

3.2.4 *The shore station*

The onshore facilities consist of two separate buildings: the power hut and the shore station. The power hut is located close to the place where the MEOC arrives on land and provides the power for the detector. The shore station is located in La Seyne-sur-Mer and has several rooms dedicated to the operation of ANTARES; a picture of the shore station is shown in figure 3.9.

The computer room hosts racks with DWDM boards that receive the signals from the DWDM boards of the detector. It also hosts a PC farm that performs the filtering (triggering) and stor-

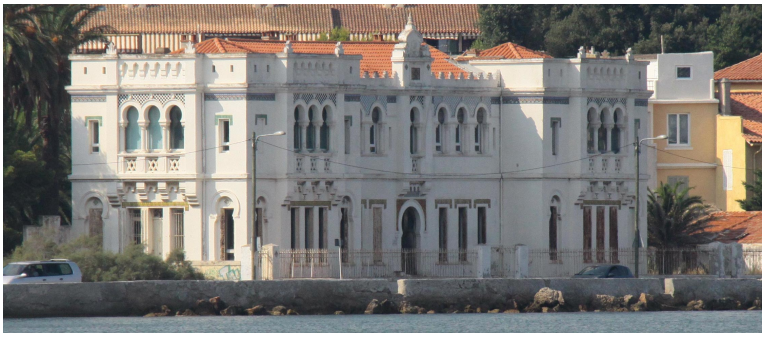

Figure 3.9: A photograph of the shore station in La Seyne-sur-Mer. Image credit Nicky, www.LaSeyne.Info.

age of the data. On average, the trigger reduces the data flow by a factor of about 10000. The filtered data are written in the ROOT format [Antcheva et al., 2009], and are copied to the IN2P3 computing centre in Lyon overnight.

The control room contains several computers for the operation of the detector and on-site shifts are performed here. Most of the shifts are performed remotely however, by means of a Virtual Network Computing (VNC) application.

3.2.5 *Calibration*

An important aspect is the calibration of the detector. In order to achieve an angular resolution of the order of a few tenths of a degree, the position of the OMs and the timing of the signals has to be known to an accuracy of 10 cm and 1 ns respectively. The calibration of the integrated charge measured by the PMTs is also important. These calibrations will now be described in more detail.

Position calibration

The detector lines move in the sea currents, so it is important to monitor the (relative) positions of all the OMs. A High Frequency Long Base Line (HFLBL) acoustic system is used to monitor the positions of hydrophones on storeys 1, 8, 14, 19 and 25 of each line. The positions are obtained by triangulation using emitters in the BSS of each line and some extra emitters on the sea floor. This allows the position of each OM to be known with an accuracy of about 10 cm [Adrián-Martínez et al., 2012b]. The orientation of

the OMs is also required, which is measured with an accuracy of a few degrees using compasses and tiltmeters.

Time calibration

For time calibration, the master clock is used to measure time delays between the shore station and the LCMs. The internal LED from each OM (wavelength of 470 nm) is used to determine the time delay from the moment the PMT measures the photon to when the signal arrives at the electronics of the LCM. Furthermore, four LED beacons (wavelength of 472 nm) are placed on storeys 2, 9, 15 and 21 on each string for intra-line calibration and two laser beacons (wavelength of 532 nm) located in the BSSs of lines 7 and 8 for inter-line calibration. Using these systems, a relative time calibration between the detector elements of less than 1 ns can be achieved, which is sufficient to obtain the required angular resolution [Aguilar et al., 2011a].

Charge calibration

The integrated charge of the analogue pulse from the PMT has to be converted to the number of photo-electrons that created the pulse. This calibration is performed using dedicated runs in which the output signal of the PMT is digitised at random moments to obtain the so-called pedestal value. This is the output given by the electronics even when no signal is detected by the PMT. The Single Photo-Electron peak is then studied using minimum bias events, for which ^{40}K decays and bioluminescence can be used, since they produce primarily single photons. The knowledge of the location of the single photo-electron peak and the pedestal value can then be used to determine the charge conversion for the dynamic range of the ADC of about 20 photo-electrons.

It has been noticed that the charge measurements by the ADC are influenced by the time measurements by the TDC, an effect known as cross-talk. Using in situ measurements, this effect is corrected for.